TRAJECTORY TRACKING APPROACH FOR ORCHARD INSPECTION VEHICLE BASED ON IMM-EKF AND IMPROVED STANLEY CONTROLLER
/
基于 IMM-EKF 与改进 STANLEY 的果园巡检车轨迹跟踪方法

Junling HU [1)], Xiaofan LIU [2)], Meixia JIA [1,*)]
[1)] Chongqing Jianzhu College, School of Intelligent Manufacturing, Chongqing, China
[2)] Communication University of China, School of Economics and Management, Beijing, China;
Tel: +86 13637821418; E-mail: jiameixia23@163.com
Corresponding author: Meixia JIA
DOI: https://doi.org/10.35633/inmateh-79-70

Keywords: *orchard inspection vehicle; IMM-EKF; pose correction; trajectory tracking*

ABSTRACT
To address the instability of trajectory tracking in unmanned orchard inspection vehicles caused by satellite navigation signal attenuation and track slippage, an integrated control method based on pose correction and an improved Stanley controller was proposed. First, a pose-correction algorithm based on the interacting multiple-model extended Kalman filter (IMM-EKF) was developed. By incorporating the nonlinear dynamic characteristics of tracked vehicles, the algorithm improved the robustness of pose estimation under varying motion states and measurement conditions. Second, an improved Stanley trajectory-tracking controller incorporating feedforward control and dynamic parameter adjustment was designed based on the corrected pose estimates. By accounting for path curvature in advance, the controller optimized the control commands and reduced lateral and heading errors. Simulations conducted using the Robot Operating System (ROS) platform and field tests performed in an actual vineyard were used to evaluate the proposed method. At a representative operating speed of 1.0 m/s, the mean lateral error during continuous multi-route trajectory tracking was 0.019 m, and the mean root-mean-square error (RMSE) was 0.021 m. These results demonstrate that the proposed method can improve trajectory-tracking accuracy, stability, and smoothness under the tested orchard conditions.

摘要
针对果园复杂环境下卫星导航信号衰减与履带滑移引起的无人巡检车轨迹跟踪不稳定问题，本文提出了一种基于位姿修正与改进 Stanley 算法的综合控制方法。首先，构建了基于交互式多模型扩展卡尔曼滤波（IMM-EKF）的位姿修正算法。该算法结合履带车辆非线性动力学特征，提高了车辆在运动状态和观测条件变化下的位姿估计鲁棒性。其次，基于修正后的位姿数据，设计了一种融合前馈控制策略与动态参数调整的改进 Stanley 轨迹跟踪控制器。该控制器通过提前考虑路径曲率信息，对轨迹跟踪控制指令进行优化，从而减小横向误差与航向误差。基于机器人操作系统（Robot Operating System, ROS）平台的仿真分析与真实葡萄园环境下的实车试验结果表明，在 1 m/s 的典型作业速度下，车辆在多路线连续轨迹跟踪中的平均横向误差为 0.019 m，平均均方根误差（RMSE）为 0.021 m。结果表明，所提方法在测试果园条件下能够提高车辆轨迹跟踪的精度、稳定性与平顺性。

INTRODUCTION
As Chinese agricultural transformation and upgrading progresses, the automation and intelligentisation of orchard operations have become key means of alleviating labour shortages and reducing production costs (*Gao et al., 2021*). However, orchard environments are highly complex and unstructured, featuring undulating terrain, canopy obstruction and variable soil physicochemical properties, which pose a significant challenge to the autonomous navigation capabilities of unmanned inspection vehicles *(Xue et al., 2023)*. Recent studies from different agricultural regions have shown that orchard rows and dense tree canopies can seriously affect satellite-based navigation. Dense orchard canopies may prevent the reliable use of GPS signals *(Durand-Petiteville et al., 2018)*, and accurate robot localisation with respect to orchard row centre lines remains challenging because satellite signals are often obstructed by foliage *(Fei et al., 2022)*. Intermittent GNSS dropout in orchards can also significantly degrade navigation accuracy and requires auxiliary localisation methods such as LiDAR or INS *(Li et al., 2024)*. Particularly in complex orchard terrain, Global Navigation Satellite System (GNSS) signals are often attenuated or interrupted due to vegetation cover; coupled with the inherent slippage of tracked chassis when travelling on unpaved surfaces, this makes it difficult for traditional

navigation systems to provide continuous, high-precision position and attitude data, thereby leading to system oscillations and instability in trajectory tracking control.

For tracked and wheeled agricultural vehicles, track–soil and wheel–soil slip represent important sources of motion uncertainty. Slip estimation has been shown to be essential for the path-tracking control of autonomous agricultural vehicles operating on wet and deformable soils *(Han et al., 2019)*. In addition, kinematic models incorporating both translational slip and rotational slippage have been developed for trajectory prediction in tracked agricultural robots *(Zhao et al., 2024)*. These findings indicate that pose estimation, slip modelling, and trajectory tracking should be considered jointly when developing autonomous navigation systems for orchard inspection vehicles.

Stable, high-precision pose estimation is the cornerstone of autonomous navigation *(Zhou et al., 2021*). At present, autonomous navigation systems commonly employ data fusion techniques combining GNSS and Inertial Navigation Systems (INS) to compensate for the limitations of single GNSS signals; however, due to cost constraints on orchard operation vehicles, low-to-medium accuracy INS systems are highly prone to accumulating drift errors during prolonged signal blockage, making it difficult to meet high-precision positioning requirements *(Lv et al., 2025)*. In terms of filtering algorithms, the Extended Kalman Filter (EKF) is widely used for state estimation and noise filtering in non-linear systems; however, filters based on a single motion model struggle to accurately capture the complex non-linear dynamic behaviour of a vehicle under variable road conditions *(Zhang et al., 2014)*. To this end, the Interactive Multi-Model (IMM) algorithm demonstrates excellent adaptability to system behaviour, thanks to its ability to dynamically switch between multiple motion hypotheses *(Nie et al., 2021)*. The deep integration of IMM with the Extended Kalman Filter (EKF) enables effective addressing of the challenge of high-precision pose estimation for orchard operation vehicles under complex constraints.

In the field of trajectory tracking control, the Stanley algorithm is widely used for lateral control in autonomous vehicles due to its geometric intuitiveness and computational efficiency *(Thrun et al., 2006).* In response to the time-varying and uncertain nature of agricultural scenarios, many researchers have introduced improved geometric control, fuzzy control, optimisation algorithms and model predictive control (MPC) to enhance the tracking performance of agricultural vehicles *(Kayacan et al., 2015; Plessen and Bemporad, 2017; Wang et al., 2022; Xu et al., 2022).* For example, improved Stanley controllers have been used to reduce path-tracking errors of autonomous tractors, while MPC-based methods have been adopted to handle actuator constraints and improve tracking stability in agricultural machinery. However, the narrow row spacing, uneven terrain and frequent curved sections within orchards require the control system to be more proactive and robust. Existing improved methods still have limitations in terms of transient smoothness, adaptability to variable ground conditions, and tracking accuracy on curved paths *(AbdElmoniem et al., 2020; Wang et al., 2022).*

To address navigation challenges in complex orchards, this study proposes an integrated control framework combining IMM-EKF for precise pose correction and an improved feedforward Stanley algorithm. The proposed method uses IMM-EKF to reduce pose fluctuation caused by GNSS signal degradation and vehicle motion uncertainty, and introduces curvature feedforward into the Stanley controller to improve tracking response on curved paths. Simulations and field trials verify that this method can improve the accuracy, smoothness, and reliability of vehicle trajectory tracking under the tested orchard conditions.

To address navigation challenges in complex orchards, this study proposes an integrated control framework combining IMM-EKF for precise pose correction and an improved feedforward Stanley algorithm. Simulations and field trials verify that this method significantly enhances the accuracy, smoothness, and reliability of the vehicle trajectory tracking.

MATERIALS AND METHODS

Using dual-antenna GNSS-RTK positioning technology, the vehicle is able to determine its global position through absolute positioning. However, in real-world orchards, vehicles often need to operate in complex environments characterised by uncertainty and dynamic changes *(Zhou et al., 2014)*. For example, signal instability or unavailability caused by tree cover may affect the accuracy and reliability of absolute positioning. To overcome these challenges, this study introduces an attitude correction technique based on the Interactive Multiple Model Extended Kalman Filter (IMM-EKF). The IMM framework provides an adaptive state-estimation strategy for systems with switching motion modes or time-varying uncertainty by combining multiple model hypotheses according to their posterior probabilities (*Blom and Bar-Shalom, 1988; Li and Jilkov, 2005*). By integrating the IMM framework with the estimation capability of the EKF in nonlinear systems, the IMM-EKF can improve the robustness of vehicle pose estimation under varying motion and measurement conditions (*Jwo et al., 2013*). Specifically, at each time step, the IMM-EKF first calculates the mixed initial state of each model based on the model transition probability and the state estimate from the previous time step. Then, each EKF sub-filter performs state prediction and measurement update. Finally, the posterior probability of each model is updated according to the measurement likelihood, and the EKF estimates are weighted and combined to obtain the integrated state estimate at the current time. The architecture of the IMM-EKF algorithm is shown in Figure 1.

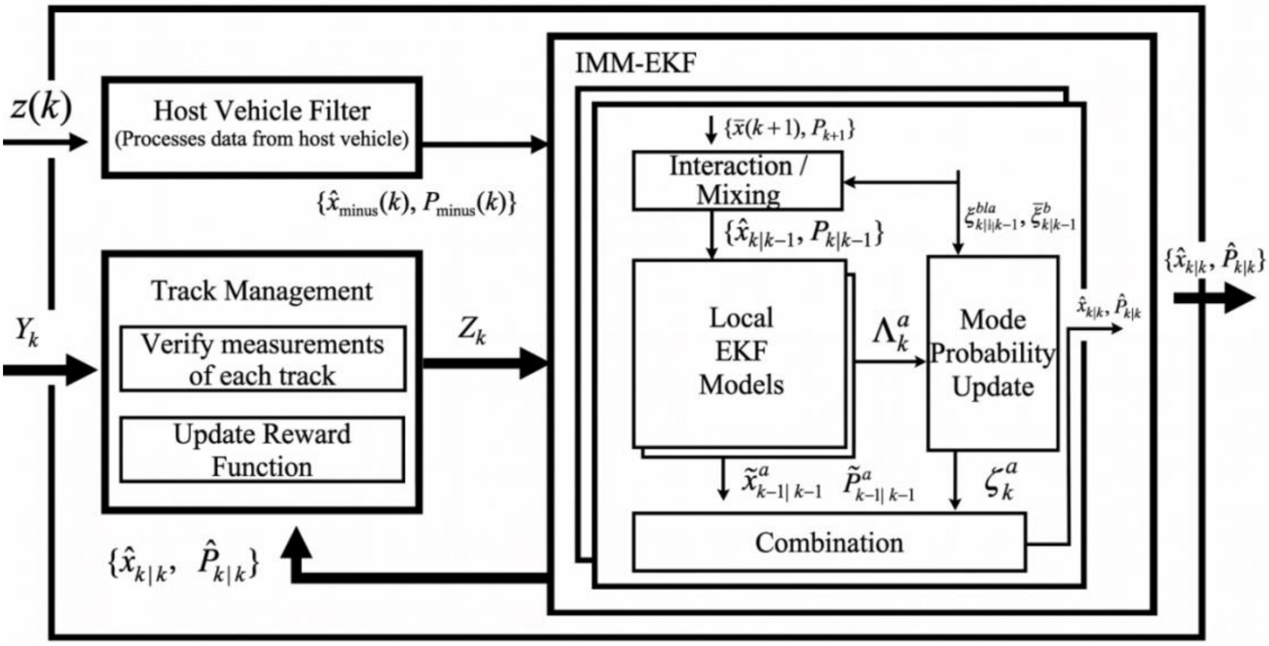

Fig. 1 - IMM-EKF algorithm architecture

This study employs a dual-antenna GNSS-RTK (Global Navigation Satellite System-Real Time Kinematic) system to obtain the vehicle's global position and attitude data. The system is based on real-time dynamic carrier phase differential technology. By calculating the relative positions of the master and slave antennas, it is capable of outputting high-precision global coordinates (longitude, latitude and altitude) as well as the vehicle's three-dimensional attitude angles (heading, pitch and roll) in real time *(Zhang et al., 2022)*.

To meet the requirements for subsequent non-linear dynamic modelling and trajectory tracking control, the system uses a standard Direction Cosine Matrix (DCM) to map the geodetic Cartesian coordinate system data obtained from GNSS-RTK to the local horizontal coordinate system *(Shan et al., 2018)*. Following the coordinate transformation, the absolute coordinates (x, y) and heading angle θ of the orchard operation vehicle in the planar coordinate system are extracted. These three state variables will serve directly as the initial observation inputs for the subsequent Interactive Multi-Model Extended Kalman Filter (IMM-EKF), which is designed to address signal attenuation and noise interference in environments where the signal is obscured by orchard canopies *(Wu et al., 2021)*.

The vehicle pose in the local planar coordinate frame is selected as the system state. The angular velocities of the left and right drive sprockets are treated as the control inputs, whereas the corresponding slip ratios and the vehicle slip angle are regarded as time-varying model parameters. These variables are used to characterize the effects of track slip on the vehicle motion *(Yang et al., 2022)*.

At discrete time step *k*, the longitudinal position, lateral position, and yaw angle of the tracked inspection vehicle are combined into the state vector:

$$\mathbf{x}_k = \begin{bmatrix} x_k \\ y_k \\ \theta_k \end{bmatrix} \tag{1}$$

where x_k and y_k denote the global longitudinal and lateral coordinates of the vehicle, respectively, in m, and θ_k denotes the vehicle yaw angle in rad, measured counterclockwise from the positive direction of the global *X*-axis.

The control input $\mathbf{u}_k$ (comprising the angular velocities of the left and right drive sprockets) and the slip-related parameter vector $\boldsymbol{\eta}_k$ are respectively defined as:

$$\mathbf{u}_k = \begin{bmatrix} \omega_{l,k} \\ \omega_{r,k} \end{bmatrix}, \boldsymbol{\eta}_k = \begin{bmatrix} i_{l,k} \\ i_{r,k} \\ \alpha_k \end{bmatrix} \tag{2}$$

Here, $i_{l,k}$ and $i_{r,k}$ are the real-time slip ratios of the left and right tracks, respectively, and α_k is the vehicle slip angle. Accordingly, the discrete-time nonlinear state equation is written as:

$$\mathbf{x}_{k+1} = f(\mathbf{x}_k, \mathbf{u}_k, \boldsymbol{\eta}_k) + \mathbf{w}_k \tag{3}$$

where $\mathbf{w}_k$ denotes the process noise.

Since the GNSS-RTK system directly measures the vehicle pose (x_k, y_k, θ_k), the observation model is linear, and its Jacobian is given by:

$$\mathbf{H}_k = \left.\frac{\partial h(\mathbf{x})}{\partial \mathbf{x}}\right|_{\mathbf{x}=\mathbf{x}_{k|k-1}} = \mathbf{I}_3 = \begin{bmatrix} 1 & 0 & 0 \\ 0 & 1 & 0 \\ 0 & 0 & 1 \end{bmatrix} \tag{4}$$

Since the standard prediction and measurement-update equations of the EKF are well established, they are not repeated here. In this study, the system nonlinearity mainly arises from the state-transition model $f(\cdot)$ whereas the observation model is linear, with $H_k = I_3$. Therefore, the following discussion focuses on the covariance prediction and the Jacobian matrix of the nonlinear state-transition model *(Yang et al., 2015)*.

On this basis, in order to quantify the uncertainty in the forecast, the process of updating the forecast state covariance P requires the introduction of a process noise covariance matrix, the calculation of which can be expressed as:

$$P_{k+1} = A_k P_k A_k^T + Q_k \tag{5}$$

Here, A_k is the Jacobian matrix of the system's dynamic model based on the current state estimate, reflecting how minute changes in the system's state variables affect the evolution of the system's overall state.

$$A_k = \begin{bmatrix} 1 & 0 & A_{K13} \\ 0 & 1 & A_{K23} \\ 0 & 0 & 1 \end{bmatrix} \tag{6}$$

$$A_{K13} = -\frac{r\left(\left(1-i_l\right)w_l + \left(1-i_r\right)w_r\right)(\sin(\theta) + \cos(\theta)\tan(\alpha))}{2} \tag{7}$$

$$A_{K23} = \frac{r\left(\left(1-i_l\right)w_l + \left(1-i_r\right)w_r\right)(\cos(\theta) - \sin(\theta)\tan(\alpha))}{2} \tag{8}$$

In particular, A_{K13} and A_{K23} are based on a vehicle kinematic model, taking into account the effects of slip ratio and wheel speed on changes in vehicle direction, and reveal the complexity of the interactions between state variables in a non-linear dynamic system.

$$Q_k = \begin{bmatrix} \sigma_{w_l}^2 & 0 & 0 \\ 0 & \sigma_{w_r}^2 & 0 \\ 0 & 0 & \sigma_\theta^2 \end{bmatrix} \tag{9}$$

$$P_k = \begin{bmatrix} \sigma_x^2 & 0 & 0 \\ 0 & \sigma_y^2 & 0 \\ 0 & 0 & \sigma_\theta^2 \end{bmatrix} \quad (10)$$

The process noise covariance accounts for the influence of random noise from various sources in real-world driving conditions—such as wheel speed noise and steering noise—on state estimation.

Based on the standard IMM framework, the weights of each motion model are dynamically updated using the model transition probability matrix, and the posterior probability is calculated using the likelihood function, ultimately outputting the fused optimal state estimate and covariance matrix.

In order to precisely control the vehicle movement along the desired path whilst performing a path-tracking task, it is essential to accurately calculate the path-tracking error, including lateral and heading errors. These errors serve as key indicators of the deviation between the vehicle's current state and its desired trajectory, and are crucial for designing effective control strategies.

Lateral error refers to the perpendicular distance between the vehicle's current position and the nearest point on the intended path. Let the actual position of the vehicle be denoted by (x_v, y_v), and determine the projection point (x_p, y_p) of the vehicle's current position onto the desired path, as shown in Figure 2.

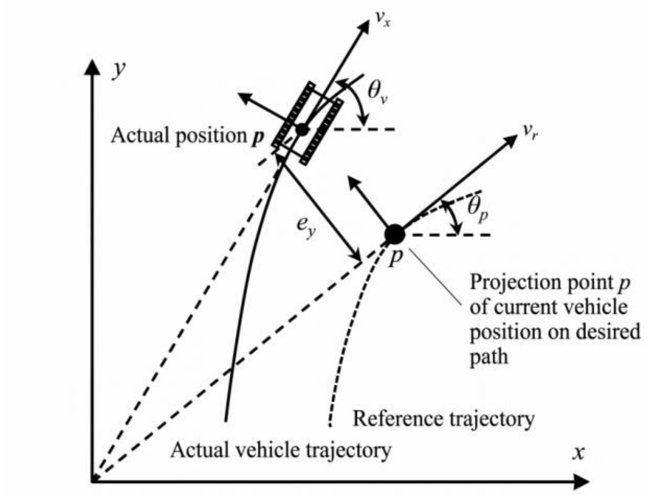

Fig. 2 - The correlation between the actual driving trajectory and the reference trajectory of the vehicle.

The lateral error e_y is given by the distance between the vehicle's actual position and its projected position on the desired path; the mathematical expression is:

$$e_y = \sqrt{(x_v - x_p)^2 + (y_v - y_p)^2} \cdot \mathrm{sgn}(y_v - f(x_v)) \quad (11)$$

Here, $\mathrm{sgn}(\cdot)$ is a sign function used to determine the direction of the error (whether the vehicle is to the left or right of the desired path). Heading error refers to the angular difference between the vehicle's current heading and the tangent direction of the desired path at its projection point. Let θ_v be the vehicle's actual heading angle; the tangent angle θ_p at the projection point (x_p, y_p) on the desired path can be obtained by differentiating $f'(x_p)$:

$$\theta_p = \arctan(f'(x_p)) \quad (12)$$

The course error e_θ can then be calculated as:

$$e_\theta = \theta_v - \theta_p, \quad e_\theta \in (-\pi, \pi] \quad (13)$$

The pose compensation module calculates the deviation between the actual trajectory and the desired trajectory, and adjusts the control inputs accordingly to achieve more precise trajectory tracking.

The expected trajectory can be expressed as a function:

$$y_r = f(x_r) \quad (14)$$

(x_r, y_r) denotes a point on the desired trajectory. The lateral error e_y and heading error e_θ between the vehicle's actual position and its desired position are defined as:

$$e_y = y - f(x) \tag{15}$$

$$e_\theta = \theta - \tan^{-1}(f'(x)) \tag{16}$$

Here, $f'(x)$ is the derivative of the expected trajectory at x, representing the direction of the tangent line to the trajectory.

Based on the findings of the above study, the pose estimates provided by the IMM-EKF are used to calculate the corrected lateral error $\hat{e}_y$ and heading error $\hat{e}_\theta$:

$$\hat{e}_y = \hat{y} - f(\hat{x}) \tag{17}$$

$$\hat{e}_\theta = \hat{\theta} - \tan^{-1}(f'(\hat{x})) \tag{18}$$

Using these corrected errors, a pose compensation module is designed to adjust the vehicle's control inputs in order to minimise these errors. The control input δ for pose compensation—namely, the vehicle's steering angle—can be adjusted using the following control law:

$$\delta = k_1 \cdot \hat{e}_y + k_2 \cdot \hat{e}_\theta \tag{19}$$

In this context, k_1 and k_2 are the control gains.

In order to further enhance the accuracy and stability of path tracking, the Stanley controller requires optimisation and refinement. Building upon the traditional Stanley method, the improved controller must not only accurately calculate path tracking errors but also adapt more flexibly to a variety of driving conditions, including different speeds, curvatures and changes in the external environment.

The improved Stanley control law is as follows:

$$\delta(t) = \arctan\left(\frac{k_e \cdot e_y(t)}{v(t)}\right) + k_\theta \cdot e_\theta(t) + \psi(t) \tag{20}$$

where: $e_y(t)$ - the lateral error at time t; $e_\theta(t)$ - the heading error at time t; $v(t)$ - the vehicle's speed; k_e - the adjustment coefficient for the lateral error; k_θ - the adjustment coefficient for the heading error.

Here, $\psi(t)$ represents the feedforward control term, which is expressed as follows:

$$\psi(t) = \arctan(k_\psi \cdot \frac{1}{g(t)}) \tag{21}$$

where: k_ψ — the feedforward control coefficient; $g(t)$ — the radius of curvature of the path at time t.

This control law responds directly to the current lateral and heading errors via the feedback term, whilst anticipating upcoming path changes via the feedforward term.

When designing a trajectory tracking control algorithm based on Stanley, the stability of the system must also be taken into account.

Given that the controller minimises the lateral error $\hat{e}_y$ and the yaw error $\hat{e}_\varphi$ by controlling the input δ, a Lyapunov function can be constructed to reflect these two errors, expressed as follows:

$$L = \frac{1}{2}(k_1 \hat{e}_y^2 + k_2 \hat{e}_\theta^2) \tag{22}$$

This function satisfies the condition that $L > 0$ holds for all $\hat{e}_y \neq 0$ or $\hat{e}_\varphi \neq 0$, and $L(0,0) = 0$, thereby fulfilling the first condition for a Lyapunov function.

Next, it is necessary to calculate $\dot{L}$, that is, the derivative of L with respect to time:

$$\dot{L} = k_1 \hat{e}_y \dot{\hat{e}}_y + k_2 \hat{e}_\theta \dot{\hat{e}}_\theta \tag{23}$$

Based on the system dynamics, $\dot{\hat{e}}_y$ and $\dot{\hat{e}}_\theta$ are determined by the vehicle's dynamic model and the control input δ; $\dot{\hat{e}}_y$ can be regarded as a function of lateral velocity, whilst $\dot{\hat{e}}_\theta$ can be regarded as a function of angular velocity.

Incorporating the control law into the analysis, the control input δ is designed to minimise $\hat{e}_y$ and $\hat{e}_\theta$. Stability analysis based on the Lyapunov function—namely, the expressions for $\dot{\hat{e}}_y$ and $\dot{\hat{e}}_\theta$—reveals a trend whereby the lateral and yaw errors decrease over time, thereby ensuring that the system converges within a specified error margin.

RESULTS

Precise trajectory tracking is the cornerstone of autonomous tracked vehicles, and this requires powerful and efficient algorithms.

To validate the performance and robustness of the proposed method, two simulation experiments were conducted: one involving straight-line path tracking control, and the other involving circular trajectory control.

A simulated orchard environment containing tree obstacles was created using ROS and Gazebo. A three-dimensional vehicle model with realistic physical and dynamic properties was then imported, and the sensor parameters were configured. Subsequently, a multimodel extended Kalman filter (EKF) framework was developed to fuse multisensor data. The framework dynamically updated the probability assigned to each motion model based on the observations and performed weighted fusion of the corresponding state estimates to obtain an optimal estimate of the vehicle pose. At the control level, a Stanley controller node was deployed to calculate the lateral tracking error by combining the predefined reference trajectory with the EKF-based state estimate. The controller then generated steering commands that enabled the vehicle to follow the prescribed path. Finally, RViz was used to visualize the planned and actual trajectories and the sensor outputs, as shown in Fig. 3(a). The controller and filter parameters were subsequently tuned to improve path-tracking stability, as shown in Fig. 3(b).

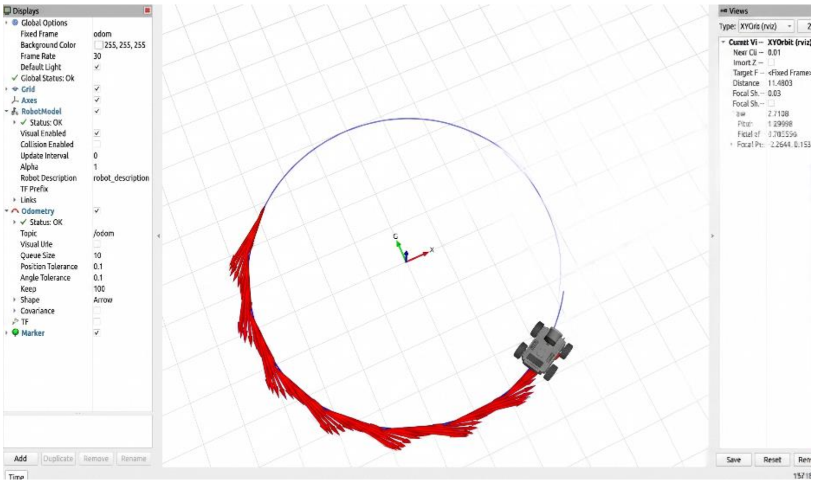

(a)

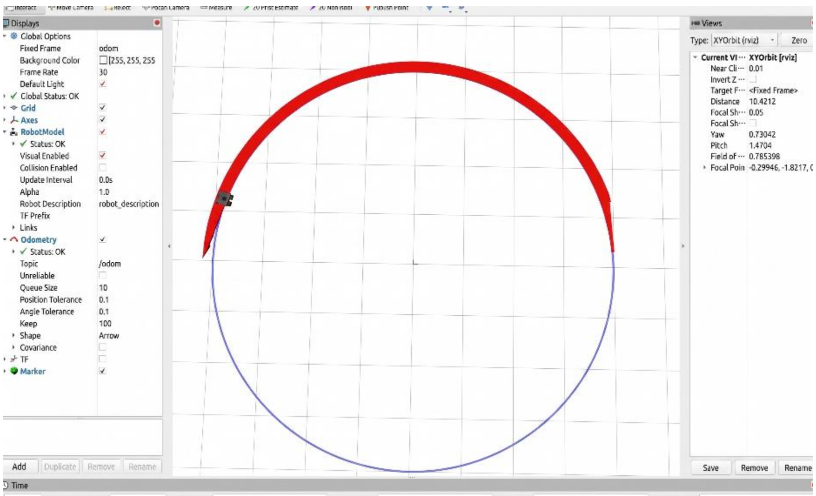

(b)

Fig. 3 - Trajectory tracking simulation experiment

To evaluate the performance of the control algorithm, different trajectory types, including straight and curved paths, were defined, and the vehicle's tracking accuracy, path-convergence rate, and robustness were assessed. The relevant state and control data were recorded by logging ROS topics during the simulation runs.

The simulation parameters were selected to reproduce real-world operating conditions as closely as possible. The vehicle's initial heading angle was set to 0.02 rad to represent the small initial orientation errors commonly encountered in practical applications. To reflect the physical constraints of an actual tracked vehicle, the maximum steering angular velocity was limited to 0.2 rad/s. In addition, the vehicle speed was set to 1.0 m/s to represent the typical low-speed operating conditions of tracked vehicles in the field.

The simulation results showed that the vehicle rapidly converged to the predefined reference path and subsequently followed it with high accuracy. However, an evaluation based solely on the mean error and standard deviation would provide an incomplete statistical characterization of tracking performance. Additional information, including the simulation duration, number of repeated runs, and confidence intervals, is required to quantify tracking stability more comprehensively.

For the straight-line path-tracking simulation shown in Fig. 4, the vehicle travelled at a constant speed of 1.0 m/s. Each simulation run lasted 120 s, and 20 independent trials were conducted to reduce the influence of random variability. The statistical results aggregated across the 20 trials were as follows: the mean lateral tracking error was 0.014 m, with a standard deviation of 0.0057 m and a 95% confidence interval of 0.0116–0.0164 m; the mean heading error was 0.002 rad, with a standard deviation of 0.0008 rad and a 95% confidence interval of 0.0017–0.0023 rad.

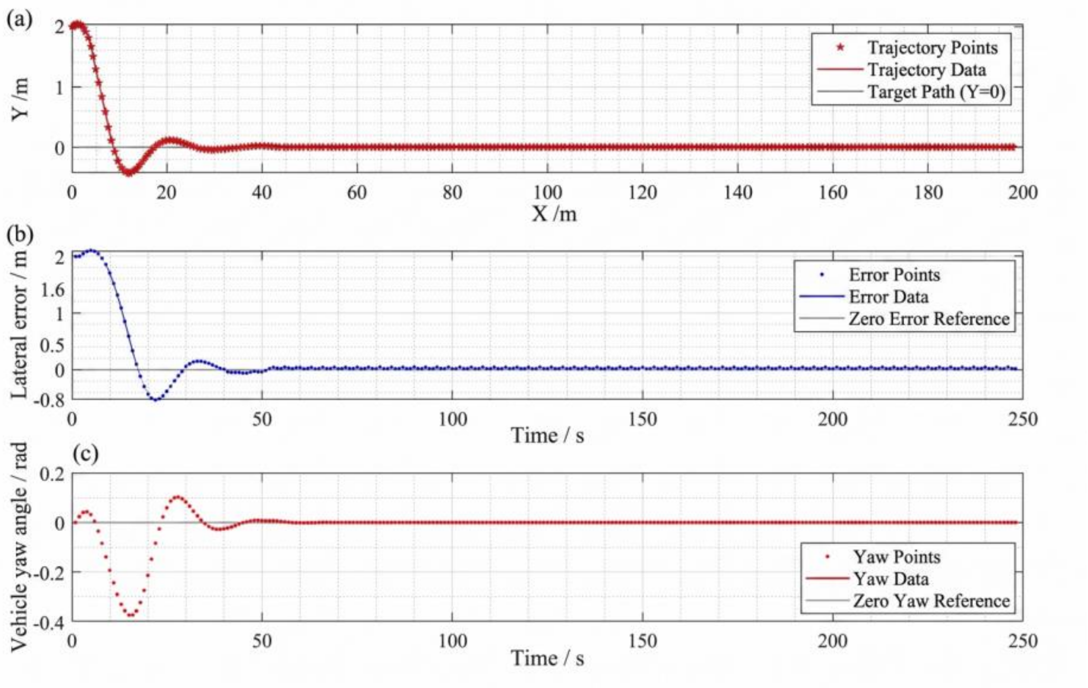

Fig. 4 - Straight-line path-tracking simulation and error.

As shown in Fig. 5, the circular trajectory-tracking simulation yielded a mean lateral error of 0.023 m, with a standard deviation of 0.0086 m, and a mean heading error of 0.033 rad, with a standard deviation of 0.021 rad. These results demonstrate that the proposed algorithm achieved accurate and stable trajectory tracking along a curved reference path.

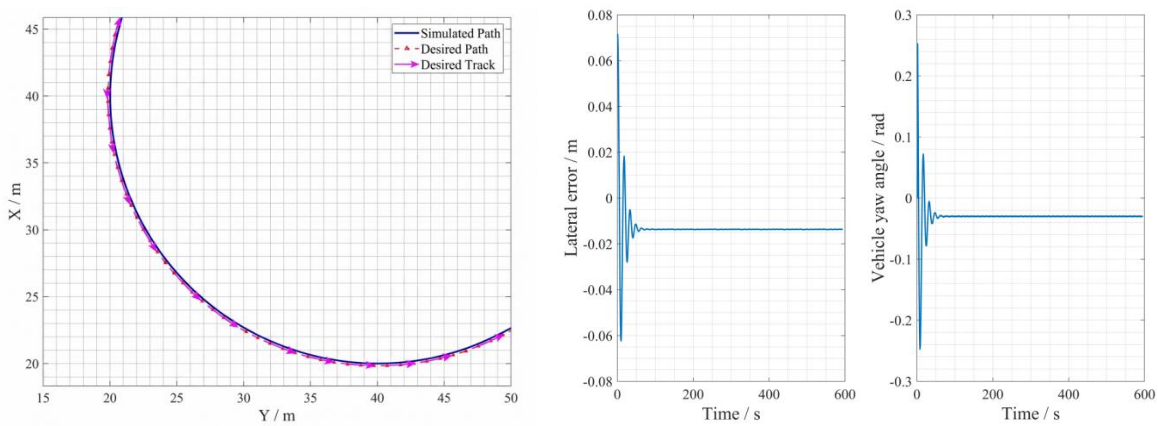

Fig. 5 - Simulated circular path-tracking error

To evaluate the effectiveness of the proposed path-tracking algorithm under real operating conditions, field experiments were conducted in a vineyard. Fig. 6 shows the test site, which featured uneven terrain and inter-row weeds. Each vine row was 100 m long, and the row spacing ranged from 3.5 to 4.0 m.

Fig. 6 - Vineyard real-field scenario

Two field tests were conducted using the tracked orchard inspection vehicle: constant-speed straight-line trajectory tracking at 1.0 m/s and continuous trajectory tracking along multiple routes. Each test condition was repeated six times to improve the statistical reliability of the results. The straight test route was 100 m long, whereas the total length of the continuous multi-route trajectory was 480 m. Standardized initial conditions were applied, with nominal position and heading offsets set to zero. Before data recording, the maximum allowable initial position and heading deviations were limited to 0.03 m and 1.5°, respectively. Data acquisition began only after the GNSS-RTK positioning solution had remained stable for 3 s at the starting point and ended when the vehicle entered the predefined coordinate threshold at the endpoint. A GNSS-RTK receiver operating at 10 Hz recorded the vehicle's real-time position and heading. The relative deviation was defined as the ratio of the instantaneous lateral tracking error to the maximum allowable lateral offset from the reference trajectory. This dimensionless metric was calculated and statistically analysed across all repeated trials.

Fig. 7 shows the continuous multi-route trajectory-tracking trials conducted in the vineyard under operating conditions representative of autonomous orchard vehicles. The reference trajectories were generated and measured using a clearly defined procedure. Discrete waypoints were manually surveyed by static GNSS-RTK measurements at the row boundaries and turning zones, and a minimum turning radius of 2.5 m was applied to all inter-row turns. Cubic B-spline interpolation was then used to convert the discrete waypoints into smooth, continuously differentiable trajectories. All trajectory data were expressed in a local horizontal Cartesian coordinate system transformed from geodetic coordinates. Before the vehicle tests, the ground-truth reference trajectories were fully surveyed using static RTK measurements. The tracked vehicle followed the preplanned smooth trajectories stably across multiple vine rows, and the recorded trajectory curves demonstrated reliable tracking accuracy over uneven vineyard terrain.

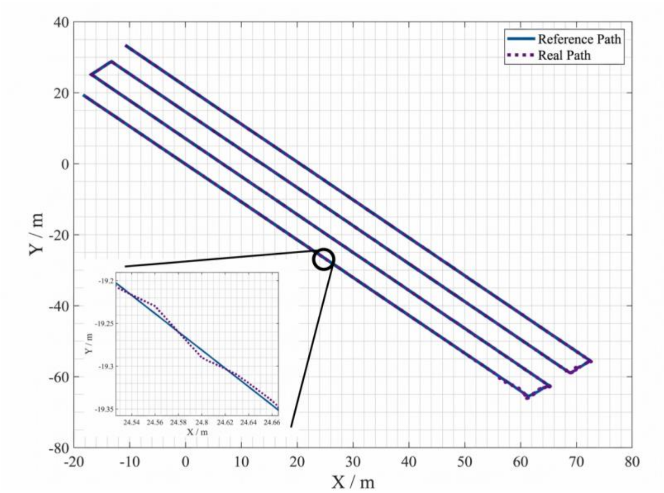

Fig. 7 - Continuous multi-route trajectory-tracking test

Fig. 8(a) shows the variation in lateral tracking error over time. The lateral error remained within 0.06 m throughout the test and exhibited increasingly stable fluctuations as the test progressed, with an apparent periodic pattern. Fig. 8(b) shows the variation in heading error over time. The heading error remained below 0.03 rad (approximately 1.72°) throughout the tracking process, indicating that the vehicle maintained stable heading alignment with the reference trajectory.

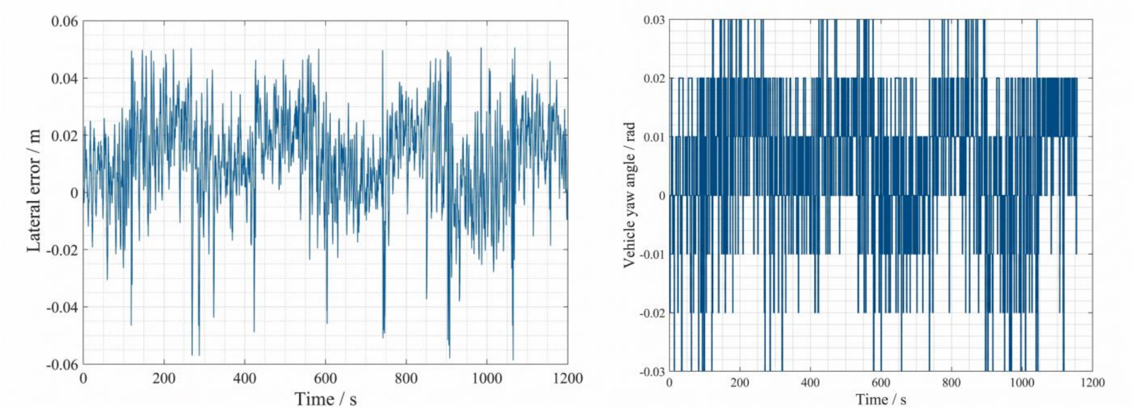

(a) Lateral tracking error over time (b) Vehicle yaw angle over time

Fig. 8 - Experimental results for continuous multi-route trajectory tracking

Analysis of the multi-route test data shown in Fig. 8 was used to quantify the tracking performance of the proposed algorithm. Across six repeated vineyard trials, the mean lateral RMSE was 0.021 m, while the steady-state heading error remained within ±0.03 rad. Compared with the baseline method combining a standard single-model EKF with the original Stanley controller, the proposed method reduced the mean lateral RMSE by 42.7% under identical vineyard conditions. The tracked vehicle maintained stable alignment with the reference trajectory and limited both lateral and heading errors to relatively low levels, demonstrating the applicability of the proposed method to vineyard navigation. Nevertheless, this study has several limitations. Only the low-speed operating condition of 1.0 m/s was evaluated, and tracking performance under severe slip or on steep terrain was not investigated.

Table 1

Statistical results for the absolute lateral tracking error during continuous multi-route trajectory tracking (Unit: meter)

Test	Maximum	Minimum	Mean	Standard deviation	RMSE
1	0.042	0.0000016	0.019	0.016	0.021
2	0.078	0.0000077	0.022	0.023	0.027
3	0.015	0.0000008	0.020	0.018	0.023
4	0.075	0.0000016	0.019	0.018	0.021
5	0.128	0.0000026	0.017	0.016	0.019
6	0.055	0.0000019	0.014	0.011	0.017

The data presented in Table 1 is derived from multiple repeated trials conducted along the planned route shown in Figure 8. To simulate real-world conditions, these trials were carried out on different dates. This approach aims to ensure that, whilst the route remains consistent, the appearance of the soil changes in the real world due to human activity and environmental influences, and that external noise, such as weather conditions, is also constantly varying.

Table 1 presents the absolute lateral-error statistics obtained from six repeated multi-route trajectory-tracking trials. An audit of the raw data identified two important inconsistencies. First, Trial 3 reported a maximum absolute lateral error of 0.015 m, together with a mean absolute error of 0.020 m and an RMSE of 0.023 m. These values are mathematically inconsistent because, for a set of non-negative absolute errors, neither the mean nor the RMSE can exceed the maximum observed value. The Trial 3 statistics were therefore recalculated.

Second, the reported minimum errors, including values such as 0.0000016 m, were below the practical measurement capability of the field GNSS-RTK system and were considered numerical noise rather than physically meaningful measurements. Accordingly, the minimum-error values were reported to a practical precision of 0.001 m.

After recalculating the trial statistics and standardizing the raw data, the aggregated results from the six tests were as follows. The mean maximum lateral error was 0.066 m, and the mean minimum detectable error, rounded to three decimal places, was 0.001 m. The overall mean absolute lateral error was 0.019 m, with a standard deviation of 0.017 m. The RMSE values for the individual trials ranged from 0.017 to 0.027 m, with a mean of 0.021 m. For every trial, the RMSE was lower than the corresponding maximum lateral error after calibration. These calibrated metrics characterize the lateral-error distribution of the proposed Stanley controller enhanced with IMM-EKF under uneven vineyard conditions and demonstrate its ability to limit lateral tracking deviations under canopy-induced signal attenuation and track-slip disturbances.

CONCLUSIONS

This study developed an integrated navigation framework combining IMM-EKF-based multimodel pose correction with a feedforward-enhanced Stanley controller for tracked orchard inspection vehicles operating under GNSS signal attenuation and track-slip disturbances. Simulations and vineyard field tests demonstrated measurable improvements in trajectory-tracking performance. At a constant speed of 1.0 m/s, the straight-line simulation achieved a mean lateral error of 0.014 m, while the multi-route field trials produced a mean lateral RMSE of 0.021 m. Compared with the baseline method combining a single-model EKF with the original Stanley controller, the proposed method reduced the mean lateral RMSE by 42.7% under identical orchard conditions.

This study nevertheless has several limitations. Only one low operating speed, 1.0 m/s, was evaluated, and all field experiments were conducted in a single vineyard with relatively mild terrain irregularities. Performance under more demanding conditions, including steep slopes and severe track slip, was not investigated, and the method was not cross-validated using different vehicle chassis. Future work will therefore focus on extending the method to variable-speed operation, conducting additional tests on sloped and highly slippery orchard terrain, integrating LiDAR- and vision-based positioning to reduce long-term localization drift, and evaluating the generalizability of the framework across different types of tracked agricultural vehicles. Overall, the proposed method provides experimentally supported guidance for centimetre-level autonomous trajectory tracking by unmanned orchard vehicles.

ACKNOWLEDGEMENT

This work was supported by the Science and Technology Research Project of Chongqing Municipal Education Commission (Grant No. KJQN202504305).

REFERENCES

[1] Abd Elmoniem, Osama A., Abdelaziz M., Maged S. A. (2020). A path-tracking algorithm using predictive Stanley lateral controller. *International Journal of Advanced Robotic Systems*, vol. 17, no. 6. DOI: 10.1177/1729881420974852.

[2] Bar-Shalom Y., Li X. R., Kirubarajan T. (2001). Estimation with Applications to Tracking and Navigation: Theory, Algorithms and Software. *John Wiley & Sons.* DOI: 10.1002/0471221279.

[3] Blom H. A. P., Bar-Shalom Y. (1988). The interacting multiple model algorithm for systems with Markovian switching coefficients. *IEEE Transactions on Automatic Control*, vol. 33, no. 8, pp. 780–783. DOI: 10.1109/9.1299.

[4] Durand-Petiteville A., Le Flecher E., Cadenat V., Sentenac T., Vougioukas S. (2018). Tree detection with low-cost three-dimensional sensors for autonomous navigation in orchards. *IEEE Robotics and Automation Letters*, vol. 3, no. 4, pp. 3876–3883. DOI: 10.1109/LRA.2018.2857005.

[5] Fei Z., Vougioukas S. (2022). Row-sensing templates: A generic 3D sensor-based approach to robot localization with respect to orchard row centerlines. *Journal of Field Robotics*, vol. 39, pp. 712–738. DOI: 10.1002/rob.22072.

[6] Gao P., Jiang J., Song J., Xie F., Bai Y., Fu Y., Wang Z., Zheng X., Xie S., Li B. (2021). Fruit Tree Model Reconstruction Method for Robotic Canopy Volume Measurement in Orchards. *IEEE Access*, vol. 9, pp. 156246–156259. DOI: 10.1109/ACCESS.2021.3127566.

[7] Grewal M. S., Andrews A. P., Bartone C. G. (2020). Global Navigation Satellite Systems, *Inertial Navigation, and Integration. 4th Edition. John Wiley & Sons.* DOI: 10.1002/9781119547860.

[8] Han X., Kim H. J., Jeon C. W., Yi S. Y., Moon H. C., Kim J. H. (2019). Application of a 3D tractor-driving simulator for slip estimation-based path-tracking control of auto-guided tillage operation. *Biosystems Engineering*, vol. 178, pp. 70–85. DOI: 10.1016/j.biosystemseng.2018.11.003.

[9] Jwo D. J., Chung F. C., Yu K. L. (2013). GPS/INS integration accuracy enhancement using the interacting multiple model nonlinear filters. *Journal of Applied Research and Technology*, vol. 11, no. 4, pp. 496–509. DOI: 10.1016/S1665-6423(13)71557-8.

[10] Kayacan E., Kayacan E., Ramon H., Saeys W. (2015). Towards agrobots: Identification of the yaw dynamics and trajectory tracking of an autonomous tractor. *Computers and Electronics in Agriculture*, vol. 115, pp. 78–87. DOI: 10.1016/j.compag.2015.05.012.

[11] Li X. R., Jilkov V. P. (2005). Survey of maneuvering target tracking. Part V: Multiple-model methods. *IEEE Transactions on Aerospace and Electronic Systems*, vol. 41, no. 4, pp. 1255–1321. DOI: 10.1109/TAES.2005.1561886.

[12] Li Y., Feng Q., Ji C., Sun J., Sun Y. (2024). GNSS and LiDAR integrated navigation method in orchards with intermittent GNSS dropout. *Applied Sciences*, vol. 14, no. 8, Article 3231. DOI: 10.3390/app14083231.

[13] Plessen M. M. G., Bemporad A. (2017). Reference trajectory planning under constraints and path tracking using linear time-varying model predictive control for agricultural machines. *Biosystems Engineering*, vol. 153, pp. 28–41. DOI: 10.1016/j.biosystemseng.2016.10.019.

[14] Shan T., Englot B. (2018). LeGO-LOAM: Lightweight and ground-optimized LiDAR odometry and mapping on variable terrain. Proceedings of the *2018 IEEE/RSJ International Conference on Intelligent Robots and Systems (IROS), Madrid, Spain*, pp. 4758–4765. DOI: 10.1109/IROS.2018.8594299.

[15] Thrun S., Montemerlo M., Dahlkamp H., Stavens D., Aron A., Diebel J., Fong P., Gale J., Halpenny M., Hoffmann G., Lau K., Oakley C., Palatucci M., Pratt V., Strohband S., Dupont C., Jendrossek L. E., Koelen C., Markey C., Rummel C., van Niekerk J., Jensen E., Alessandrini P., Bradski G., Davies B., Ettinger S., Kaehler A., Nefian A., Mahoney P. (2006). Stanley: The robot that won the DARPA Grand Challenge. *Journal of Field Robotics*, vol. 23, no. 9, pp. 661–692. DOI: 10.1002/rob.20147.

[16] Wang L., Zhai Z., Zhu Z., Mao E. (2022). Path tracking control of an autonomous tractor using improved Stanley controller optimized with multiple-population genetic algorithm. *Actuators*, vol. 11, no. 1, Article 22. DOI: 10.3390/act11010022.

[17] Wu J., Ma X., Peng T., Wang H. (2021). An improved timed elastic band (TEB) algorithm of autonomous ground vehicle (AGV) in complex environment. *Sensors*, vol. 21, no. 24, Article 8312. DOI: 10.3390/s21248312.

[18] Xu J., Lai J., Guo R., Lu X., Xu L. (2022). Efficiency-oriented MPC algorithm for path tracking in autonomous agricultural machinery. *Agronomy*, vol. 12, no. 7, Article 1662. DOI: 10.3390/agronomy12071662.

[19] Xue G., Li R., Zhang Z., Liu R. (2023). State-of-the-art and tendency of SLAM algorithms based on 3D LiDAR. *Information and Control*, vol. 52, no. 1, pp. 18–36. DOI: 10.13976/j.cnki.xk.2023.2254.

[20] Yang J., Chung S. J., Hutchinson S., Johnson D., Kise M. (2015). Omnidirectional-vision-based estimation for containment detection of a robotic mower. Proceedings of the *2015 IEEE International Conference on Robotics and Automation (ICRA)*, Seattle, USA, pp. 6344–6351. DOI: 10.1109/ICRA.2015.7140090.

[21] Yang L., Xu Y., Liang Y., Qin J., Li Y., Wang X., Zhai W., Wen L., Chen Z., Wu C. (2022). Extraction of straight field roads between farmlands based on agricultural vehicle-mounted LiDAR. *International Journal of Agricultural and Biological Engineering*, vol. 15, no. 5, pp. 155–162. DOI: 10.25165/j.ijabe.20221505.6933.

[22] Zhang X., Zhu T., Du L., Hu Y., Liu H. (2022). Local path planning of autonomous vehicle based on an improved heuristic Bi-RRT algorithm in dynamic obstacle avoidance environment. *Sensors*, vol. 22, no. 20, Article 7968. DOI: 10.3390/s22207968.

[23] Zhao X., Lu E., Tang Z., Luo C., Xu L., Wang H. (2024). Trajectory prediction method for agricultural tracked robots based on slip parameter estimation. *Computers and Electronics in Agriculture*, vol. 222, Article 109057. DOI: 10.1016/j.compag.2024.109057.

[24] Zhou K., Leck Jensen A., Sørensen C. G., Busato P., Bochtis D. D. (2014). Agricultural operations planning in fields with multiple obstacle areas. *Computers and Electronics in Agriculture*, vol. 109, pp. 12–22. DOI: 10.1016/j.compag.2014.08.013.

[25] Zhou Q., Zhang H., Li Y., Li Z. (2015). An adaptive low-cost GNSS/MEMS-IMU tightly-coupled integration system with aiding measurement in a GNSS signal-challenged environment. *Sensors*, vol. 15, no. 9, pp. 23953–23982. DOI: 10.3390/s150923953.